



This is a repository copy of *Constrained multi-scale turnover Lagrangian map for anisotropic synthetic turbulence: A priori tests*.

White Rose Research Online URL for this paper:  
<http://eprints.whiterose.ac.uk/97391/>

Version: Published Version

---

**Article:**

Li, Y. and Rosales, C. (2014) Constrained multi-scale turnover Lagrangian map for anisotropic synthetic turbulence: A priori tests. *Physics of Fluids*, 26 (7). ARTN 075102. ISSN 1070-6631

<https://doi.org/10.1063/1.4890322>

---

**Reuse**

Unless indicated otherwise, fulltext items are protected by copyright with all rights reserved. The copyright exception in section 29 of the Copyright, Designs and Patents Act 1988 allows the making of a single copy solely for the purpose of non-commercial research or private study within the limits of fair dealing. The publisher or other rights-holder may allow further reproduction and re-use of this version - refer to the White Rose Research Online record for this item. Where records identify the publisher as the copyright holder, users can verify any specific terms of use on the publisher's website.

**Takedown**

If you consider content in White Rose Research Online to be in breach of UK law, please notify us by emailing [eprints@whiterose.ac.uk](mailto:eprints@whiterose.ac.uk) including the URL of the record and the reason for the withdrawal request.



[eprints@whiterose.ac.uk](mailto:eprints@whiterose.ac.uk)  
<https://eprints.whiterose.ac.uk/>



## Constrained multi-scale turnover Lagrangian map for anisotropic synthetic turbulence: A priori tests

Yi Li and Carlos Rosales

Citation: [Physics of Fluids \(1994-present\)](#) **26**, 075102 (2014); doi: 10.1063/1.4890322

View online: <http://dx.doi.org/10.1063/1.4890322>

View Table of Contents: <http://scitation.aip.org/content/aip/journal/pof2/26/7?ver=pdfcov>

Published by the [AIP Publishing](#)

---

### Articles you may be interested in

[Hybrid simulations of metal particle nucleation: A priori and a posteriori analyses of the effects of unresolved scalar interactions on nanoparticle nucleation](#)

Phys. Fluids **24**, 075110 (2012); 10.1063/1.4737660

[Multifractal subgrid-scale modeling for large-eddy simulation. I. Model development and a priori testing](#)

Phys. Fluids **17**, 075111 (2005); 10.1063/1.1965058

[Toward improved consistency of a priori tests with a posteriori tests in large eddy simulation](#)

Phys. Fluids **17**, 015103 (2005); 10.1063/1.1823511

[A priori testing of wall models for separated flows](#)

Phys. Fluids **15**, 3048 (2003); 10.1063/1.1606681

[A priori subgrid analysis of temporal mixing layers with evaporating droplets](#)

Phys. Fluids **12**, 1573 (2000); 10.1063/1.870405

---



**AIP** | Journal of  
Applied Physics

*Journal of Applied Physics* is pleased to  
announce **André Anders** as its new Editor-in-Chief

# Constrained multi-scale turnover Lagrangian map for anisotropic synthetic turbulence: *A priori* tests

Yi Li<sup>1,a)</sup> and Carlos Rosales<sup>2,b)</sup>

<sup>1</sup>*School of Mathematics and Statistics, University of Sheffield, Sheffield S3 7RH, United Kingdom*

<sup>2</sup>*Department of Mechanical Engineering, Universidad Tecnica Federico Santa Maria, Valparaiso, Chile*

(Received 25 March 2014; accepted 3 July 2014; published online 22 July 2014)

Synthetic turbulence has been useful in the modelling and simulation of turbulence, and as a surrogate to understand the dynamics of real hydrodynamic turbulence. In a recently proposed Multiscale Turnover Lagrangian Map (MTLM) method, an initial random field is transformed into a synthetic field after a series of simple mappings, with moderate computational cost. It has been shown that the resulted fields reproduce highly realistic statistics on many aspects of isotropic hydrodynamic turbulence, including small-scale intermittency, geometric statistics, and pressure statistics. Thus, it is of great interests to generalize the method to model inhomogeneous turbulence. In this paper, we formulate the problem as an optimization problem, where the initial random field is taken as the control variable, and the additional features presented in inhomogeneous turbulence are taken as a target function to be matched by the synthetic fields. The goal is to find the optimal control variable which minimizes the difference between the target function and the synthetic field. Using the adjoint formulation, we derive the optimality system of the problem, which formulates a procedure to generate inhomogeneous synthetic turbulence. The procedure, named the Constrained MTLM, is applied to synthesize two Kolmogorov flows where persistent large scale structures produce nontrivial mean flow statistics and local anisotropy in small scales. We compare the synthetic fields with direct numerical simulation data, and show that the former reproduces closely the mean flow statistics such as Reynolds stress distribution and mean turbulent kinetic energy balance. They also reproduce the effects of inhomogeneity on small scale structures, which is manifested in the distributions of mean subgrid-scale energy dissipation, and the alignment between the subgrid-scale stress tensor and the filtered strain rate tensor, among others. We conclude that the method is useful to further extend the applicability of synthetic turbulence. © 2014 AIP Publishing LLC. [<http://dx.doi.org/10.1063/1.4890322>]

## I. INTRODUCTION

Synthetic turbulence refers to stochastic fields that possess characteristics of real hydrodynamic turbulent flows, and that are usually generated by ways more cost-efficient compared with solving the Navier-Stokes (NS) equations. The interest in synthetic turbulence has been motivated by two different applications. On one hand, it provides a suitable framework for numerical experimentations aiming at determining the smallest set of dynamical processes that still allow the manifestation or modelling of features distinctive of real turbulence. In that way, it helps to shed light on internal mechanisms of turbulence that have not yet been well understood. Different approaches have been developed from this perspective, aiming at modelling different aspects of turbulent flows. Some have

a) Author to whom correspondence should be addressed. Electronic mail: [yili@sheffield.ac.uk](mailto:yili@sheffield.ac.uk)

b) Electronic mail: [carlos.rosales@usm.cl](mailto:carlos.rosales@usm.cl)

focused on small-scale intermittency.<sup>1,2</sup> Others have focused on subgrid-scale (SGS) dissipation and interscale interactions,<sup>3,4</sup> or temporal correlation properties, which are important for modelling particle dispersion.<sup>5–7</sup>

On the other hand, the evolution of Large-Eddy simulation (LES) towards applications in increasingly complex flows has brought with it the need for more sophisticated means of prescribing the turbulent characteristics of the flow at inlet boundaries. Thus, as a matter of practical interests, synthetic turbulence has also been used to generate initial and inlet boundary conditions for numerical simulations (for a review of other techniques, see, e.g., Refs. 8 and 9). **Most synthetic turbulence models are based on combination of Fourier modes,**<sup>10–14</sup> which are rescaled to comply with a target spectrum. In order to produce the required anisotropic turbulent Reynolds stress,<sup>15</sup> turbulent fluctuations are then rescaled at each point according to given Reynolds stress distribution. Different rescaling techniques have been proposed,<sup>12,16–20</sup> most of which are based on certain matrix decomposition (such as the Cholesky decomposition) of the Reynolds stress tensor. A different line of research is based on the superposition of vortices at random positions in the inlet plane, and with random orientation. These vortices are given a Langevin random walk in order to develop fluctuations in time.<sup>21</sup> A derivative of this procedure is the Synthetic-Eddy Method (SEM),<sup>22–24</sup> in which the eddies are convected at the inlet plane with a constant velocity characteristic of the flow.

When applied as inlet conditions, all the methods mentioned still require, at different degrees, a zone of redeveloping of the turbulence inside the computational domain, and there is a strong need for improvements. A novel approach has been proposed in two recent studies,<sup>25,26</sup> followed on from related works.<sup>27,28</sup> The authors show that realistic synthetic isotropic turbulent fields can be generated by the so-called Multi-scale Minimal Lagrangian Map (MMLM), and the Multi-scale Turnover Lagrangian Map (MTLM). **Starting from a random field, the mappings allow the fluid particles to advect freely over short time scales while maintaining incompressibility and the energy spectrum.** When the advections are applied over a set of nested grids with increasing resolution, it is shown that the synthetic fields not only reproduce accurately the multi-scaling properties of small scale turbulence, but also many properties related to small-scale geometrical structures as well as the pressure field. Using the synthetic fields as initial conditions for simulations, more realistic time evolution can be obtained for time evolving problems, and initial transient period can be significantly shortened for stationary problems.<sup>25</sup> It has been generalized to the synthesis of scalar fields.<sup>29</sup> The pressure field associated with the velocity field is also further investigated.<sup>30</sup>

Given its many desirable properties, one may ask if it is possible to generalize the MTLM method to anisotropic turbulence, which is more relevant to practical applications. In this paper, we propose a generalization to the MTLM that is able to accommodate anisotropic flow features. As is explained above, the MTLM method applies a mapping to a random field and obtain a realistic synthetic field. We propose to formulate the procedure as an optimization problem, where the input (the random field) serves as the control variable, and the additional features we aim to produce is taken as a target function to be matched by the synthetic fields. By solving the optimization problem, we find the optimal random field that gives us the desirable synthetic field.

In what follows, we first give a brief introduction to the MTLM method, in Sec. II. We reformulate slightly some of the steps in the procedure to facilitate the derivation of the optimization problem. We then formulate the optimization problem and derive the optimality system and explain its solution in Sec. III. Two test cases are examined in Sec. IV, where the results are discussed. Some derivations are given in details in the Appendix.

## II. THE MULTISCALE TURNOVER LAGRANGIAN MAP

We start with a brief introduction of the Multiscale Turnover Lagrangian Map.<sup>26</sup> The main building block of the procedure is the Riemann equation

$$\partial_t \mathbf{u} + (\mathbf{u} \cdot \nabla) \mathbf{u} = 0$$

which describes the velocity field of a collection of particles when the inter-particle interactions are neglected. The solution at time  $t$  is  $\mathbf{u}_t(\mathbf{x}) = \mathbf{u}(\mathbf{y})$  where  $\mathbf{y}$  is the initial location of the fluid particle which locates at  $\mathbf{x}$  at time  $t$ , i.e.,  $\mathbf{x} = \mathbf{y} + t\mathbf{u}(\mathbf{y})$ . Thus, the dynamics can be represented by an operator

$\mathcal{A}$ , which maps  $\mathbf{u}(\mathbf{y})$  to  $\mathbf{u}_t(\mathbf{x})$ , with the advection time  $t$  as a parameter.  $\mathbf{u}_t(\mathbf{x})$  is usually a highly distorted, non-Gaussian field, even if  $\mathbf{u}(\mathbf{y})$  is a Gaussian random velocity field. Thus, operator  $\mathcal{A}$  is the key ingredient that enables the MTLM method to reproduce the non-Gaussian statistics in turbulence.

Operator  $\mathcal{A}$  will be called the advection operator. In its numerical implementation, we use its integral expression, given as follows:

$$\mathcal{A}\mathbf{u}(\mathbf{x}) = \int W(\mathbf{x} - \mathbf{y} - \mathbf{u}(\mathbf{y})t) \mathbf{u}(\mathbf{y}) d^3\mathbf{y}, \quad (1)$$

where  $W(\mathbf{x})$  is a weighting function. When  $W(\mathbf{x})$  is the Dirac- $\delta$  function  $\delta(\mathbf{x})$ , we recover the definition above. In our numerical implementation,  $W(\mathbf{x})$  is approximated as follows:  $W(\mathbf{x}) = C/|\mathbf{x}|$  when  $|\mathbf{x}| \leq \ell$ , and  $W(\mathbf{x}) = 0$  when  $|\mathbf{x}| > \ell$ , where  $\ell$  is the grid size, and  $C$  is a normalization constant, ensuring the sum of the weights is unit.<sup>25</sup>

To facilitate later exposition, we define a few more operators. The filtering operator  $\mathcal{G}$  is defined in a standard way: for an arbitrary velocity field  $\mathbf{u}(\mathbf{x})$ , we have

$$\mathcal{G}\mathbf{u}(\mathbf{x}) = \int G(\mathbf{x} - \mathbf{y}) \mathbf{u}(\mathbf{y}) d^3\mathbf{y}, \quad (2)$$

where  $G$  is the cut-off filter with a given filter length. We also use the projection operator  $\mathcal{P}$ , which is defined by

$$\mathcal{P}\hat{\mathbf{u}}(\mathbf{k}) = [I - \hat{\mathbf{k}} \otimes \hat{\mathbf{k}}] \hat{\mathbf{u}}(\mathbf{k}), \quad (3)$$

where  $\hat{\mathbf{u}}(\mathbf{k})$  is the Fourier transform of  $\mathbf{u}(\mathbf{x})$ ,  $\mathbf{k}$  is the wavenumber, and  $\hat{\mathbf{k}} = \mathbf{k}/|\mathbf{k}|$ . The projection operator removes the divergence of the operand. Finally, the rescaling operator  $\mathcal{R}$  is defined by

$$\mathcal{R}\hat{\mathbf{u}}(\mathbf{k}) = \left( \frac{E_p(k)}{E_u(k)} \right)^{1/2} \hat{\mathbf{u}}(\mathbf{k}), \quad (4)$$

in which  $E_u(k)$  is the energy spectrum of  $\hat{\mathbf{u}}(\mathbf{k})$  at  $k = |\mathbf{k}|$ , and  $E_p(k)$  is a prescribed one. The output of  $\mathcal{R}$  is a velocity field with energy spectrum given by  $E_p(k)$ .  $E_p(k)$  typically is extracted from direct numerical simulation (DNS) data or analytic approximations.

Note that  $\mathcal{G}$  and  $\mathcal{P}$  are both linear operators. On the other hand,  $\mathcal{A}$  and  $\mathcal{R}$  are highly nonlinear.

We now give a brief summary of the MTLM procedure. The input to the procedure is a random velocity field  $\boldsymbol{\varphi}(\mathbf{x})$  and the prescribed energy spectrum  $E_p(k)$ , and the output is an isotropic synthetic velocity field with  $E_p(k)$  as its energy spectrum. As a first step,  $\boldsymbol{\varphi}(\mathbf{x})$  is projected onto the divergence-free subspace, giving  $\mathbf{u}_{10}(\mathbf{x}) \equiv \mathcal{P}\boldsymbol{\varphi}(\mathbf{x})$ . The procedure then defines a hierarchy of  $M$  scales  $\ell_n = 2^{-n}L$  ( $n = 1, 2, \dots, M$ ), where  $L$  is a reference length at the order of the integral length scale. Each scale  $\ell_n$  corresponds to one iteration, which takes as input the velocity field generated from the previous iteration, and generate a new velocity field.

As a consequence, following  $\boldsymbol{\varphi}$ , we have  $M + 1$  velocity fields after  $M$  iterations:  $\mathbf{u}_{10}, \mathbf{u}_{20}, \dots, \mathbf{u}_{M0}$ , and  $\mathbf{u}_e$ , where  $\mathbf{u}_e$  is the final velocity field, and  $\mathbf{u}_{n0}$  is the output of the  $(n - 1)$ th iteration and the input for the  $n$ th iteration.

In each iteration, the advection operator, the projection operator, and the rescaling operator are applied successively to the input velocity field. More specifically, supposing we start with  $\mathbf{u}_{n0}$  (hence in the  $n$ th iteration), the following operators are applied:

1.  $\mathbf{u}_{n0}$  is low-pass filtered to generate  $\mathbf{u}_{n1} \equiv \mathcal{G}_n \mathbf{u}_{n0}$ , where  $\mathcal{G}_n$  represents the filtering operation with length scale  $\ell_n$ . Note the high wavenumber components of  $\mathbf{u}_{n0}$  are kept unchanged.
2. Advection operator  $\mathcal{A}_n$ , which is  $\mathcal{A}$  with advection time equal  $t_n$  associated with  $\ell_n$ , and the projection operator  $\mathcal{P}$  are then applied to  $\mathbf{u}_{n1}$   $m_n$  times. Let the resultant velocity field be  $\mathbf{u}_{n2}$ , then  $\mathbf{u}_{n2} \equiv (\mathcal{P}\mathcal{A})^{m_n} \mathbf{u}_{n1}$ . The advection time  $t_n$  and  $m_n$  are specified below.
3.  $\mathbf{u}_{n2}$  is rescaled, giving  $\mathbf{u}_{n3} = \mathcal{R}_n \mathbf{u}_{n2}$ , where  $\mathcal{R}_n$  denotes the rescaling operator associated with  $\mathbf{u}_{n2}$ .
4.  $\mathbf{u}_{n3}$  is then merged with the high wavenumber components of  $\mathbf{u}_{n0}$  to generate the final velocity field of current iteration, which is also the initial field for the next iteration, i.e.,  $\mathbf{u}_{(n+1)0}$  (or the

final field  $\mathbf{u}_e$ ). Mathematically, we have

$$\mathbf{u}_{(n+1)0} = \mathbf{u}_{n3} + \mathcal{G}_n^c \mathbf{u}_{n0},$$

where  $\mathcal{G}_n^c = 1 - \mathcal{G}_n$ .

Combining the operations together, we may write

$$\mathbf{u}_{(n+1)0} = [\mathcal{R}_n(\mathcal{P}\mathcal{A}_n)^{m_n} \mathcal{G}_n + \mathcal{G}_n^c] \mathbf{u}_{n0}. \quad (5)$$

Hence, the final field  $\mathbf{u}_e$  is given by

$$\mathbf{u}_e = \mathcal{M}\boldsymbol{\varphi}, \quad (6)$$

where

$$\mathcal{M} = \prod_{n=1}^M [\mathcal{R}_n(\mathcal{P}\mathcal{A}_n)^{m_n} \mathcal{G}_n + \mathcal{G}_n^c] \mathcal{P}. \quad (7)$$

The product is ordered such that from left to right  $n$  decreases from  $M$  to 1.

Several parameters need to be specified before the description is complete. The advection time scale  $t_n$  in the operator  $\mathcal{A}_n$  is determined by the condition that the associated Courant-Friedrichs-Lewy number is unit, that is,

$$t_n = \frac{\ell_n}{u'_n}, \quad \text{where } u'_n = \left( \frac{2}{3} \int_0^{k_{c,n}} E_p(k) dk \right)^{1/2}.$$

$u'_n$  is the root-mean-square (rms) velocity for the low-pass filtered velocity field, and  $k_{c,n} = \pi/\ell_n$  is the cut-off wavenumber corresponding to  $\ell_n$ .

Let  $\epsilon$  be the energy dissipation rate corresponding to the prescribed energy spectrum, then the eddy turnover time scale  $\tau_n$  at scale  $\ell_n$  is given by

$$\tau_n = \frac{\ell_n^{2/3}}{\epsilon^{1/3}}. \quad (8)$$

As is explained in Rosales and Meneveau,<sup>26</sup> the application of the operator  $\mathcal{A}_n$  has to be repeated so that accumulated advection time is at the order of  $\tau_n$ . Hence, we have

$$m_n = \tau_n / t_n. \quad (9)$$

Note here both  $u'_n$  and  $m_n$  are calculated from the prescribed energy spectrum, whereas in Rosales and Meneveau<sup>26</sup> they are calculated from the generated velocity field. Our computations show that no difference is observed, presumably because the spectrum of the velocity field for most of the time is the same as the prescribed one. However, the modification greatly simplifies the derivation of the optimality system to be discussed in Sec. III.

The synthetic fields generated by the procedure has been studied in previous works,<sup>26</sup> where it is shown that the multi-scaling properties of the velocity as well as pressure fields are reproduced to high accuracy.

### III. CONSTRAINED MTLM

#### A. The optimization problem and the optimality system

Given the many desirable properties of the MTLM synthetic fields, we attempt to generalize the method to model additional features in more complex flow fields. To formulate the problem, we suppose a velocity field  $\mathbf{w}(\mathbf{x})$  is known, and our goal is to model some of its features with a modified MTLM synthetic velocity field.

To accomplish the task, one may try to modify the MTLM procedure, i.e., modify the operator  $\mathcal{M}$ . However, we observe that  $\mathbf{u}_e$  may be adjusted by tuning  $\boldsymbol{\varphi}$  too. So far,  $\boldsymbol{\varphi}$  has always been assumed to be a random Gaussian field, but it does not have to be so. Therefore, we conjecture that

it is possible to find an initial field  $\boldsymbol{\varphi}$  such that  $\mathbf{u}_e$  matches the desirable features of  $\mathbf{w}(\mathbf{x})$  and, in the meantime, maintains its other realistic features.

Such an initial field can be found via an optimization procedure. Let  $\mathcal{F}$  be a filtering operator that extracts some particular features of a velocity field. To be concrete, we assume for the moment  $\mathcal{F}$  is a cut-off filter with a large filter scale. We thus define a cost function

$$J(\mathbf{u}_e) = \frac{1}{2} \|\mathcal{F}[\mathbf{u}_e(\mathbf{x}) - \mathbf{w}(\mathbf{x})]\|^2. \quad (10)$$

We seek to minimize  $J$  over all possible  $\boldsymbol{\varphi}(\mathbf{x})$ , subject to the constraint  $\mathbf{u}_e = \mathcal{M}\boldsymbol{\varphi}$ , i.e., Eq. (6). The operator  $\mathcal{F}$  shows that the optimization procedure will only modify the large scale structures of  $\mathbf{u}_e$ . In the terminologies of flow optimization,  $\boldsymbol{\varphi}$  is the control variable, and  $\mathbf{u}_e$  is the state variable. The constraint is also called the state equation.<sup>31</sup>

The optimal solution for  $\boldsymbol{\varphi}$  can be found as part of the solution of the coupled optimality system, which includes the constraint (Eq. (6)), the adjoint equation, and the optimality condition.<sup>31</sup> Introducing a Lagrangian multiplier  $\boldsymbol{\xi}(\mathbf{x})$  (also called adjoint variable), we form the Lagrangian of the system

$$\mathcal{L}(\mathbf{u}_e, \boldsymbol{\varphi}, \boldsymbol{\xi}) = J(\mathbf{u}_e) + \int \boldsymbol{\xi} \cdot (\mathbf{u}_e - \mathcal{M}\boldsymbol{\varphi}) d^3\mathbf{x}. \quad (11)$$

The adjoint equation is given by the condition that functional derivative of  $\mathcal{L}$  with respect to the state variable  $\mathbf{u}_e$  equals zero. Following the standard technique,<sup>31</sup> we find that the adjoint equation reads

$$\boldsymbol{\xi}(\mathbf{x}) = -\mathcal{F}[\mathbf{u}_e(\mathbf{x}) - \mathbf{w}(\mathbf{x})]. \quad (12)$$

We have used  $\mathcal{F}^+\mathcal{F} = \mathcal{F} = \mathcal{F}^+$ , where  $\mathcal{F}^+$  is the adjoint operator of  $\mathcal{F}$ . The relation is true when  $\mathcal{F}$  is, e.g., a cut-off filter.

The optimality condition states that the partial functional derivative of  $\mathcal{L}$  with respect to the control variable  $\boldsymbol{\varphi}$  is zero at the optimum. To find the derivative, we use Eqs. (10) and (11), and find

$$\left. \frac{\delta \mathcal{L}}{\delta \boldsymbol{\varphi}} \right|_{\mathbf{u}_e, \boldsymbol{\xi}} = - \int \boldsymbol{\xi} \cdot \frac{\delta \mathcal{M}\boldsymbol{\varphi}}{\delta \boldsymbol{\varphi}} d^3\mathbf{x}. \quad (13)$$

Details of further derivation are given in the Appendix, where it is shown that

$$\left. \frac{\delta \mathcal{L}}{\delta \boldsymbol{\varphi}} \right|_{\mathbf{u}_e, \boldsymbol{\xi}} = -\mathcal{M}^+\boldsymbol{\xi}, \quad (14)$$

where formally  $\mathcal{M}^+$  is the adjoint operator of  $\mathcal{M}$  (or the adjoint of the tangent operator of  $\mathcal{M}$ ), defined as

$$\mathcal{M}^+ = \mathcal{P} \prod_{n=1}^M (\mathcal{B}_n + \mathcal{G}_n^c) = \mathcal{P} \sum_{i=1}^M \mathcal{G}_{i-1}^c \prod_{n=i}^M \mathcal{B}_n, \quad (15)$$

where the operators in the products are ordered such that  $n$  increases from left to right.  $\mathcal{G}_0^c$  is understood as the identity operator, and  $\mathcal{B}_n$  is defined by

$$\mathcal{B}_n = \mathcal{G}_n \mathcal{D}_n^{A+} \mathcal{D}_n^{R+}. \quad (16)$$

$\mathcal{D}_n^{R+}$  and  $\mathcal{D}_n^{A+}$  are the adjoint operators of the linearization of  $\mathcal{R}_n$  and  $(\mathcal{P}\mathcal{A}_n)^{m_n}$ , respectively. Their expressions are given in the Appendix. Note that they depend on the intermediate velocity fields generated during the MTLM procedure (i.e., when solving Eq. (6) for  $\mathbf{u}_e$ ).

The total derivative of the cost function with respect to  $\boldsymbol{\varphi}$ , denoted as  $\mathcal{D}J/\mathcal{D}\boldsymbol{\varphi}$ , can also be found. Since the adjoint equation and the state equation are solved exactly, we have<sup>31</sup>

$$\frac{\mathcal{D}J}{\mathcal{D}\boldsymbol{\varphi}} = \left. \frac{\delta \mathcal{L}}{\delta \boldsymbol{\varphi}} \right|_{\mathbf{u}_e, \boldsymbol{\xi}}, \quad (17)$$

which equals to  $-\mathcal{M}^+\boldsymbol{\xi}$  in our system. Thus, it can be calculated once  $\boldsymbol{\xi}$  and the operator  $\mathcal{M}^+$  are known.



The above results show that the optimality condition becomes

$$\mathcal{M}^+\xi = 0. \quad (18)$$

Equations (6), (12), and (18) together constitute the optimality system for the optimization problem. The solution of the system provides an optimal initial field  $\varphi$  so that the MTLM procedure produces a synthetic field that matches the desired features in a target flow field. In what follows, we called the procedure Constrained MTLM (CMTLM).

## B. Solution of the optimality system

Due to the strong nonlinearity of the equations, it appears unlikely to solve the optimality system by direct methods. However, it is straightforward to devise an iteration procedure. Given  $\varphi^0$ , the initial guess for  $\varphi$ , and a tolerance  $e$ , we repeat the following steps for  $i = 0, 1, 2, \dots$ :

1. Find  $\mathbf{u}_e^i$  from  $\varphi^i$  by applying the MTLM procedure on the latter, and save intermediate velocity fields (see the Appendix). Note this procedure solves the state equation [Eq. (6)].
2. Calculate the cost function  $J^i \equiv J(\mathbf{u}_e^i)$ . Exit if  $J^i < e$ , otherwise continue to the next step.
3. Find  $\xi^i$  from the adjoint equation, Eq. (12).
4. Find  $\mathcal{D}J/\mathcal{D}\varphi^i$  from  $\xi^i$  and the velocity fields saved in the first step, and update the control

$$\varphi^i - \lambda \frac{\mathcal{D}J}{\mathcal{D}\varphi^i} \rightarrow \varphi^i, \quad (19)$$

where  $\lambda$  is the stepsize.

In actual implementation, the stepsize  $\lambda$  is adjusted dynamically each iteration. It is increased by a fraction if the cost function is successfully reduced during the current iteration. If the cost function is increased however, we reduce  $\lambda$  and retry the iteration.

It is observed that the above algorithm uses the steepest descent method to update the approximate solution. Our computation shows that the iteration always converges in less than ten steps. Therefore, we have not pursued more sophisticated methods.

A few remarks on the evaluation of  $\mathcal{D}J/\mathcal{D}\varphi = -\mathcal{M}^+\xi$  are in order. The right-hand side of Eq. (15) can be re-arranged into a set of nested operations, as follows:

$$\mathcal{P}\{[\dots]\mathcal{B}_{M-2} + \mathcal{G}_{M-2}^c\}\mathcal{B}_{M-1} + \mathcal{G}_{M-1}^c\}\mathcal{B}_M. \quad (20)$$

The expression suggests finding  $\mathcal{M}^+\xi$  via the following procedure:  $\mathcal{B}_M\xi$  is evaluated and decomposed at length scale  $\ell_{M-1}$ , by filter  $\mathcal{G}_{M-1}$ , into a group of high wavenumber modes (HWMs) and a group of low wavenumber modes (LWMs). The HWMs are saved, whereas the LWMs are subjected to the operation of the next operator  $\mathcal{B}_{M-1}$ . The output from  $\mathcal{B}_{M-1}$  again is decomposed into LWMs and HWMs, at length scale  $\ell_{M-2}$ . The HWMs are then merged with the HWMs saved aside during the operation of  $\mathcal{B}_M$ , whereas the LWMs are subject to the operation of  $\mathcal{B}_{M-2}$ , and so on. The procedure is repeated until the output of  $\mathcal{B}_1$  is merged with all the HWMs without further decompositions.

The above procedure shows the elegant symmetry with the original MTLM procedure. While in MTLM the iteration is performed on finer and finer grids, the above procedure starts from the finest grid and iterates on coarser and coarser ones.

$\mathcal{B}_n$  is computed according to its definition, Eq. (16). We use the definitions for  $\mathcal{D}_n^{R+}$  and  $\mathcal{D}_n^{A+}$  given in the Appendix [Eqs. (A15) and (A18)]. The calculation of  $\mathcal{D}_n^{R+}$  is straightforward.  $\mathcal{D}_n^{A+}$  has a similar structure as the advection operator  $\mathcal{A}$ , and is evaluated in a similar way, which is explained in details in Ref. 25.

## IV. SIMULATIONS AND DISCUSSIONS

We demonstrate the applications of the CMTLM method with two Kolmogorov flows in this section. The tests are *a priori* tests in the sense that we focus on the ability of the synthetic fields to



reproduce the statistics in DNS. How the synthetic field can be used as initial or inlet conditions for large eddy simulations is left for future study.

Kolmogorov flows usually refer to turbulence in a periodic box driven by deterministic forcing at large scales, which leads to persistent anisotropic large scale circulations. In the first test, we focus on the small scale statistics and the effects of the large scale structures. A DNS and experimental study has been reported in Kang and Meneveau<sup>32</sup> (KM hereafter). We will compare the statistics of the CMTLM fields with the latter. In the second test, we look into the mean statistics of the large scale structures themselves. The CMTLM fields are compared with the hyperviscosity DNS reported in Borue and Orszag<sup>33</sup> (BO hereafter).

In each case, we need to specify the target velocity field  $\mathbf{w}$  and the operator  $\mathcal{F}$ . It is easy to check that, in both cases, the derivation in Sec. III is still valid for the operator  $\mathcal{F}$  given below.

### A. SGS dissipation and geometry in Kolmogorov flows

We consider the first case in this subsection. The DNS study is reported in KM,<sup>32</sup> in which the authors investigate the effects of large scale straining and rotation on SGS dissipation and the geometry of SGS motions.

In this Kolmogorov flow, the forcing term is proportional to the following vector field:

$$\mathbf{w}(\mathbf{x}) = A[\sin k_f y, \sin k_f x, 0], \quad (21)$$

with  $A$  a constant and  $k_f = 1$ . As a consequence, a mean field with same structure is generated in DNS. Therefore, we set our target flow as  $\mathbf{w}(\mathbf{x})$ . We note that  $k_f$  defines the scale of the target field, and  $\mathbf{w}$  is non-zero only on a set of four wavenumbers:  $\Omega = \{(1, 0, 0), (0, 1, 0), (-1, 0, 0), (0, -1, 0)\}$ .  $A$  is chosen to make sure that the energy spectrum of  $\mathbf{w}$  on  $\Omega$  matches  $E_p(k)$ , the prescribed spectrum.

$E_p(k)$  is taken from a  $256^3$  DNS of stationary turbulence with mean energy dissipation rate  $\epsilon = 0.1$ ,  $\nu = 0.0015$ , and the Taylor micro-scale Reynolds number  $Re_\lambda \approx 140$ .  $E_p(k)$  is plotted in Fig. 1, which shows a short  $k^{-5/3}$  range.

The operator  $\mathcal{F}$  is defined to be 1 on  $\Omega$ , and 0 otherwise. In other words, the cost function measures only the difference between  $\mathbf{u}_e$  and  $\mathbf{w}$  over  $\Omega$ . As a consequence,

$$\hat{\xi}(\mathbf{k}) = -[\hat{\mathbf{u}}_e(\mathbf{k}) - \hat{\mathbf{w}}(\mathbf{k})] \quad \text{when } \mathbf{k} \in \Omega \quad (22)$$

and  $\hat{\xi}(\mathbf{k}) = 0$  otherwise.

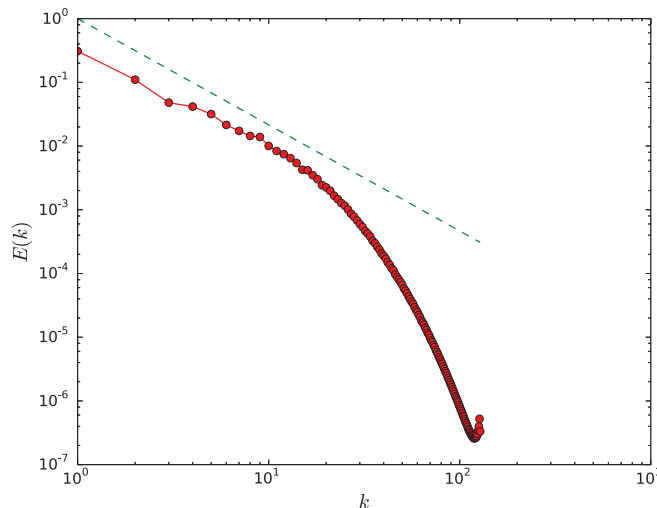


FIG. 1. The prescribed energy spectrum  $E_p(k)$ : solid line with circles. The dashed line is proportional to  $k^{-5/3}$ .

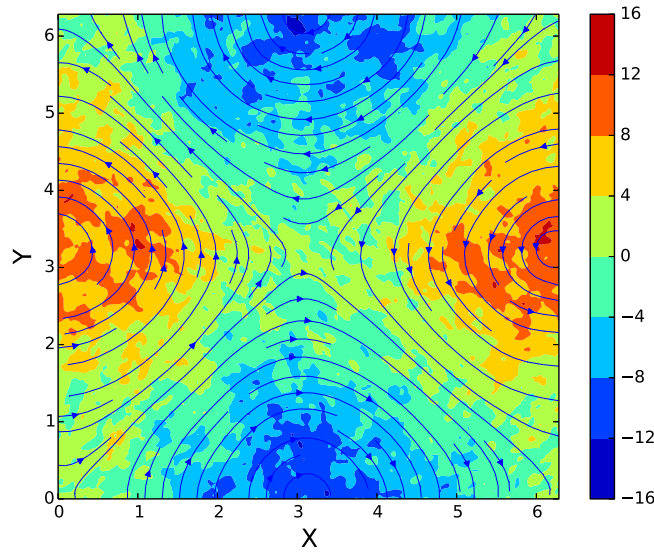


FIG. 2. The mean flow in the  $x - y$  plane. Streamlines: mean velocity. Contours: the  $z$ -component of the normalized mean vorticity.

We choose tolerance  $e = 3\%$ . The number of grid points is  $256^3$ , so that the grid size is  $\delta x = \pi/128$ . For the given parameters,  $\delta x$  is about twice the Kolmogorov length scale  $\eta = (\nu^3/\epsilon)^{1/4}$ . We set  $M = 6$  and  $L$  is chosen such that the length scales correspond to cut-off wavenumbers  $k_{c,n} = 4, 8, 16, 32, 64$ , and  $128$ .

Forty synthetic fields are generated by solving the CMTLM optimality system iteratively as described in Sec. III. All solutions are found to within tolerance in less than 10 iterations. Given that the flow fields are homogeneous in the  $z$ -direction, the statistics to be presented below are averaged over the 40 fields as well as the  $z$ -direction, unless otherwise stated. This average is denoted by pointed brackets.

### 1. Large scale structure

As expected, CMTLM is able to generate large scale structures mimicking the target flow field. This assertion is confirmed by Fig. 2, where the mean velocity field  $\langle \mathbf{u} \rangle$  is shown with streamlines and the  $\omega_z$  component of the mean vorticity  $\langle \boldsymbol{\omega} \rangle = \nabla \times \langle \mathbf{u} \rangle$  is shown in contours.  $\omega_z$  is normalized by  $\epsilon^{1/3}(\pi/k_f)^{-2/3}$ . The patterns of the streamlines follow closely what one would find from  $\mathbf{w}(\mathbf{x})$ , with a saddle in the middle of the square and centers on the boundaries. The vorticity distribution shows the two pairs of counter rotating vortices, consistent with the streamlines.

### 2. Geometry of the strain rate and SGS dissipation

Straining and rotation dominate in the saddles and centers, respectively. Such anisotropic large scale structure has significant effects on the structures of the small scales of the velocity field. We now focus on the effects of these large scale structures on SGS stresses and related quantities. The SGS stress tensor is defined as

$$\tau_{ij} = \widetilde{u_i u_j} - \widetilde{u_i} \widetilde{u_j}, \quad (23)$$

where tilde denotes low-pass filtering, and  $u_i$  is the  $i$ th component of the velocity vector. In what follows, we will use the Gaussian filter with filter scale  $\Delta$ .<sup>15</sup> A key parameter characterizing the effects of  $\tau_{ij}$  is the SGS energy dissipation, defined as<sup>15,34</sup>

$$\Pi = -\tau_{ij} \widetilde{S}_{ij}, \quad (24)$$

in which  $\widetilde{S}_{ij} = (\partial \widetilde{u_i} / \partial x_j + \partial \widetilde{u_j} / \partial x_i) / 2$  is the filtered strain rate tensor.

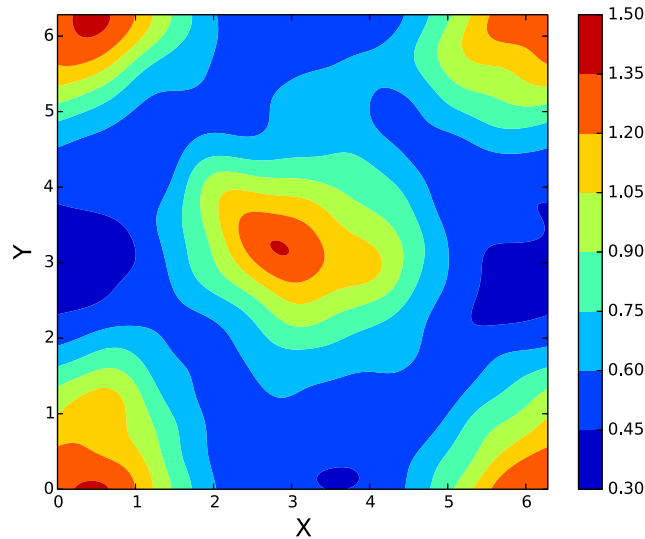


FIG. 3. Distribution of the averaged SGS dissipation rate normalized by mean energy dissipation rate:  $\langle \Pi \rangle / \epsilon$ . Filter scale  $\Delta = 64\eta$ .

The distribution of normalized mean SGS energy dissipation, i.e.,  $\langle \Pi \rangle / \epsilon$ , is shown in Fig. 3. It is observed that the peak values are observed around the saddle points of the large scale circulations, where the straining is the strongest. The peak in the middle of the flow field is elongated along the stretching directions of the saddle. On the other hand, small values are observed around the vortex centers. These features reproduce faithfully the results reported in KM.<sup>32</sup>

We look closer into the mean values for the SGS dissipations around the saddles and the centers. We calculate an aggregated mean value around the saddles (centers) by averaging  $\langle \Pi \rangle$  over a  $10 \times 10$  square around the saddles (centers). As a comparison, the aggregated mean over the whole synthetic field is also calculated. We use  $\Pi_{Ms}$ ,  $\Pi_{Mc}$ , and  $\Pi_{Mw}$  to denote these values, which are given in Table I. The numbers are consistent with Fig. 3, showing that the SGS energy dissipation is stronger around the saddle points, and weaker around the centers. Only modest difference is observed, which suggests that the effects of the large scale circulations are mostly felt by relatively large scales. Nevertheless, the comparison at the two filter scales indicates that the effect becomes stronger for larger filter scales.

The probability density functions (PDF) of  $\Pi$  for the CMTLM fields also reproduce well-known features observed in real turbulence. Fig. 4 plots the PDF of the normalized  $\Pi$  sampled over the whole synthetic field (shown with circles), and the conditional PDFs sampled around the saddles (squares) and the centers (diamonds), respectively. The PDFs display a strong positive skewness. On the other hand, a significant probability for negative fluctuations is also observed, indicating backscattering from small scales to large ones. Both again are consistent with known behaviors in real turbulence.<sup>35–37</sup> Some differences between the three PDFs are observed for large fluctuations, but they are not significant enough for definite conclusions.

The structure of the filtered strain rate tensor  $\tilde{S}_{ij}$  has been shown to correlate with the behaviors of the SGS energy dissipation.<sup>32</sup> The structure of  $\tilde{S}_{ij}$  can be characterized by the following

TABLE I. The normalized mean SGS dissipations  $\Pi_{Mi}/\epsilon$  averaged over a  $10 \times 10$  square around the saddles ( $i = s$ ), the centers ( $i = c$ ), and over the whole field ( $i = w$ ).

$\Delta/\eta$	$\Pi_{Ms}/\epsilon$	$\Pi_{Mc}/\epsilon$	$\Pi_{Mw}/\epsilon$
32	0.742	0.690	0.716
64	0.761	0.688	0.717

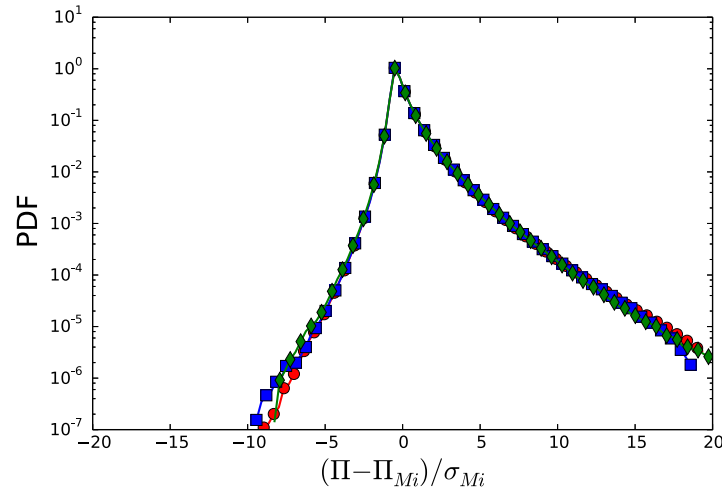


FIG. 4. The PDFs of the normalized SGS energy dissipation  $(\Pi - \Pi_{Mi})/\sigma_{Mi}$  for  $\Delta = 32\eta$ . Circles: unconditional distribution; squares: sampled in a  $10 \times 10$  square around the saddles; diamonds: sampled in a  $10 \times 10$  square around the centers.  $\Pi_{Mi}$  and  $\sigma_{Mi}$  are the respective means and standard deviations.

non-dimensional parameter:<sup>38</sup>

$$s^* = -\frac{3\sqrt{6}\alpha_s\beta_s\gamma_s}{(\alpha_s^2 + \beta_s^2 + \gamma_s^2)^{3/2}}, \quad (25)$$

where  $\alpha_s$ ,  $\beta_s$ , and  $\gamma_s$  are the eigenvalues of  $\tilde{S}_{ij}$  and  $\alpha_s \geq \beta_s \geq \gamma_s$ .  $s^*$  is bounded between  $-1$  and  $1$ , where  $s^* = -1$  corresponds to local axisymmetric contraction and  $s^* = 1$  corresponds to axisymmetric expansion. It is known that, in turbulence, the probabilistically dominant local structure corresponds to the latter.<sup>38</sup> The prediction from the synthetic CMTLM fields is given in Fig. 5, where we plot the contours of  $\langle s^* \rangle$ . Despite some statistical fluctuations, the contours show clearly that  $s^*$  tends to take larger values around the saddles in the mean flow field, whereas low values are observed near the vortex centers. The contours for high  $s^*$  in the center of the flow field are elongated along the unstable directions of the saddle. The distribution shows close correlation

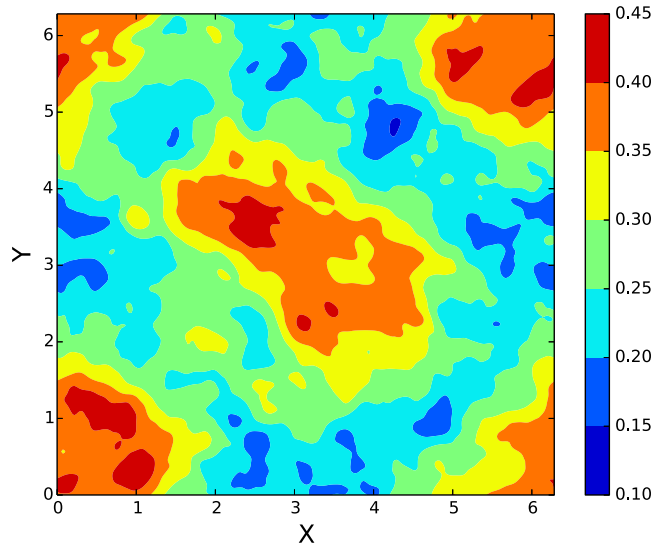


FIG. 5. The distribution of  $\langle s^* \rangle$  which characterizes the geometric structure of the filtered strain rate tensor.  $\Delta = 64\eta$ .

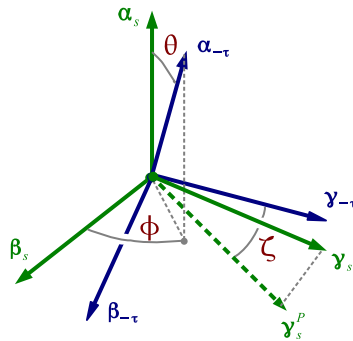


FIG. 6. The relative orientation between the eigenframes of  $\tilde{S}_{ij}$  and  $-\tau_{ij}$  is characterized by the three angles  $\theta$ ,  $\phi$ , and  $\zeta$  shown in the figure.  $\gamma_s^P$  is the projection of eigenvector  $\gamma_s$  on the  $\beta_{-\tau} - \gamma_{-\tau}$  coordinate plane.  $\theta$  and  $\phi$  are the spherical polar angles made by  $\alpha_{-\tau}$  in the eigenframe of  $\tilde{S}_{ij}$ .  $\zeta$  is the angle between  $\gamma_s^P$  and  $\gamma_{-\tau}$ .

with the distribution of  $\langle \Pi \rangle$  shown in Fig. 3. These qualitative trends are the same as what have been observed in DNS.<sup>32</sup> The magnitude of the contours are also close (see Fig. 5(c) in KM<sup>32</sup>).

### 3. Stress-strain alignment

According to Eq. (24), the behavior of  $\Pi$  is correlated with the relative alignment between the eigenframes of  $\tau_{ij}$  and  $\tilde{S}_{ij}$ . We denote the eigenvalues of  $-\tau_{ij}$ , in descending order, as  $\alpha_{-\tau} \geq \beta_{-\tau} \geq \gamma_{-\tau}$ , and corresponding normalized eigenvectors  $\alpha_{-\tau}$ ,  $\beta_{-\tau}$ ,  $\gamma_{-\tau}$ . Those of  $\tilde{S}_{ij}$  are:  $\alpha_s \geq \beta_s \geq \gamma_s$ , and  $\alpha_s$ ,  $\beta_s$ ,  $\gamma_s$ . The relative orientation of the eigenframes is described by the relative alignment of the eigenvectors.

We will look into the alignment in the CMTLM fields in comparison with the DNS fields. However, in order to obtain a complete picture, we first present the alignment data for the isotropic MTLM field. The latter has not been reported before, hence is also of interest by itself.

It is well-known that, in real hydrodynamic turbulence, there are two preferable relative orientations between the eigenframes of  $-\tau_{ij}$  and  $\tilde{S}_{ij}$ .<sup>42</sup> Using the angles  $\theta$ ,  $\phi$ , and  $\zeta$  defined in Fig. 6 to describe the relative orientation between the two frames, the above observation is demonstrated in Fig. 7. The joint PDF shows two peaks at  $(\cos \theta, \phi, \zeta) = (0.78, \pi/2, 0)$  and  $(0, 0, 0.76)$ , with peak value 2.34 and 1.65, respectively. The first peak, which we will call configuration A, corresponds to perfect alignment between  $\beta_s$  and  $\beta_{-\tau}$ , and approximately a  $39^\circ$  angle between  $\alpha_{-\tau}$  and  $\alpha_s$ . The

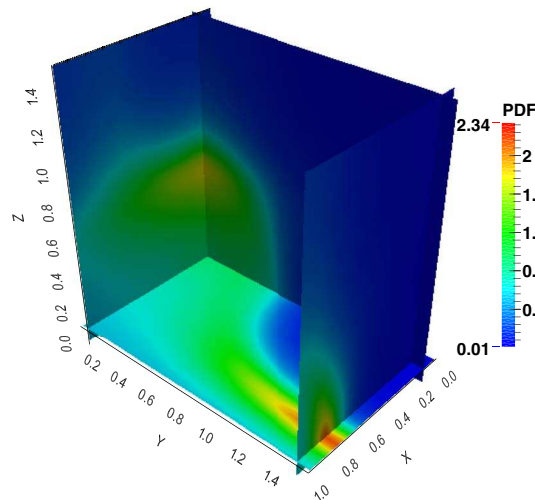


FIG. 7. Joint PDF of  $(\cos \theta, \phi, \zeta)$  for a  $256^3$  DNS data set. Filtered at  $\Delta = 32\eta$ .  $X = \cos \theta$ ,  $Y = \phi$ , and  $Z = \zeta$ .

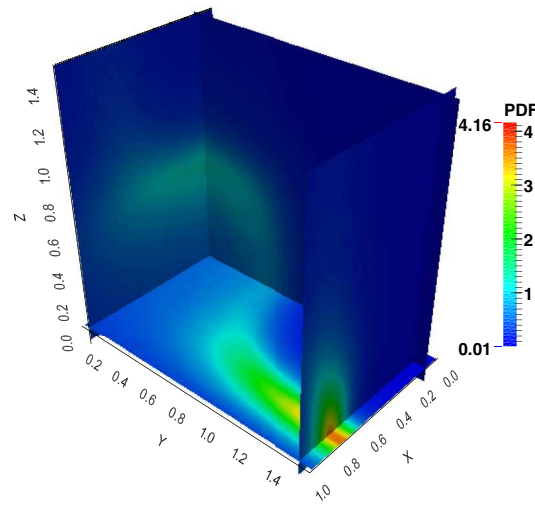


FIG. 8. Same as Fig. 7 but for MTLT fields.

second peak, configuration B, corresponds to perfect alignment between  $\alpha_{-\tau}$  and  $\beta_s$ , and a  $44^\circ$  angle between  $\gamma_{-\tau}$  and  $\gamma_s$ . The implications of these non-trivial alignment configurations have been discussed in details in previous works.<sup>42,43</sup>

The joint PDF for MTLT fields is shown in Fig. 8, where the fields are generated using the same parameters given above for the CMTLT method. It can be seen immediately that the PDF also displays two peaks. Inspection of the data shows that, the two peaks are located at  $(\cos \theta, \phi, \zeta) = (0.75, \pi/2, 0)$  and  $(0, 0, 0.71)$ , with values 4.16 and 1.22, respectively. Thus, the MTLT fields reproduce the two configurations with only slightly different angles ( $41^\circ$  for the angle between  $\alpha_{-\tau}$  and  $\alpha_s$  in configuration A, and same for the angle between  $\gamma_{-\tau}$  and  $\gamma_s$  in configuration B).

The above result reveals the ability of MTLT to reproduce the geometrical structures of SGS stresses. On the other hand, it is also observed that the peak PDF value 4.16 at configuration A is much larger than the DNS value 2.34. The deviation could be attributed to the fact that MTLT fields produce insufficient vortex tubes, as having been discussed before.<sup>26</sup>

We now discuss the results for the CMTLT fields. It turns out that the unconditional joint PDF for  $(\cos \theta, \phi, \zeta)$  in the synthetic CMTLT Kolmogorov flows displays similar trends observed in the isotropic MTLT fields (Fig. 8), i.e., we reproduce the bi-modal behavior, but also observe a over-predicted strong peak at configuration A. We thus omit the figure and focus on the conditional statistics reported in KM.<sup>32</sup> The distribution of  $\langle \Pi \rangle$  in Fig. 3 indicates that the relative orientation between the eigenvectors of  $\tau_{ij}$  and  $\tilde{S}_{ij}$  is different around the saddle and the vortex centers, which is indeed observed in KM.<sup>32</sup> For the CMTLT fields, the results are shown in Fig. 9, where we plot the PDFs of  $|\alpha_{-\tau} \cdot \alpha_s| \equiv |\cos(\alpha_{-\tau}, \alpha_s)|$  conditioned, respectively, around the saddle (circles) and the centers (squares). While the PDFs are calculated for the direction cosines, we plot them against the corresponding angles, to compare with the same result documented in KM.<sup>32</sup> Fig. 9 shows that, in the centers of the vortex, the most likely angle between  $\alpha_{-\tau}$  and  $\alpha_s$  is around  $42^\circ$ . Around the saddle,  $\alpha_{-\tau}$  and  $\alpha_s$  tend to align more closely to each other. There is a much higher probability to observe small angles, compared with in the vortex centers. This behavior is consistent with Fig. 3, since closer alignment between  $\alpha_{-\tau}$  and  $\alpha_s$  tends to increase  $\Pi$ . This general trend is also in agreement with previous findings.<sup>32</sup> There are, however, quantitative differences. For DNS data, the peak of the PDF sampled around the saddle is at  $\theta \sim 0^\circ$  (see Fig. 9(c) in KM<sup>32</sup>). On the other hand, for CMTLT data, there is a residual peak at  $\theta \approx 38^\circ$ , even though the probability distribution is shifted significantly towards small angles, as explained above.

The discrepancy is most likely due to the deficit of the MTLT procedure, which is inherited by the CMTLT fields. Because of the overestimated probability for configuration A in which  $\alpha_{-\tau}$  and  $\alpha_s$  align at the  $41^\circ$  angle, the conditional PDF in Fig. 9 has had a relatively weak peak at  $38^\circ$ .

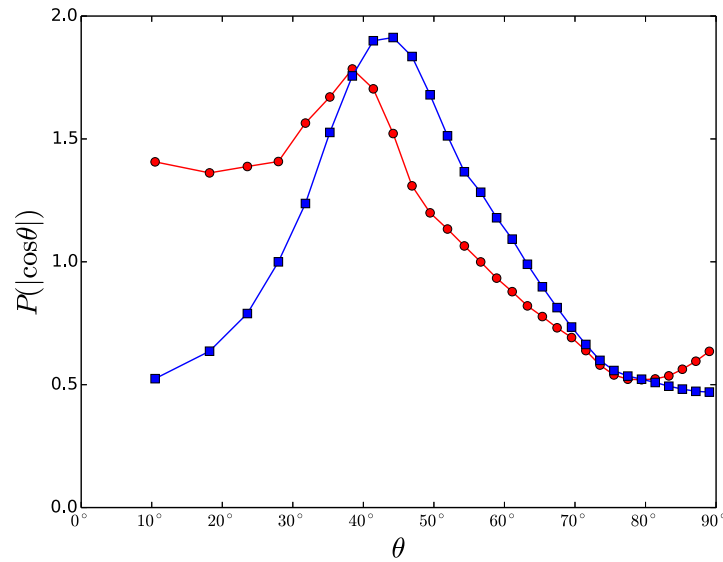


FIG. 9. The PDF of the magnitude of the direction cosine between  $\alpha_{-\tau}$  and  $\alpha_s$ :  $P(|\cos(\alpha_{-\tau}, \alpha_s)|)$ . Circle: sampled from a  $10 \times 10$  square around the saddle; squares: sampled from a  $10 \times 10$  square around the vortex centers. Filtered at  $\Delta = 128\eta$ .

#### 4. Anisotropy in the SGS stress tensor

It is also of interests to look into the geometrical structure of the SGS stress tensor  $\tau_{ij}$ . One way to inspect the geometry of  $\tau_{ij}$  is to use the so-called Anisotropy Invariant map (AIM).<sup>15,39,40</sup> Defining

$$a_{ij} = \frac{\tau_{ij}}{\tau_{kk}} - \frac{1}{3}\delta_{ij}, \quad (26)$$

which is the normalized anisotropic part of  $\tau_{ij}$ , the anisotropy of  $\tau_{ij}$  is characterized by the two invariants of  $a_{ij}$

$$\text{II} = -a_{ij}a_{ji}/2, \quad \text{III} = a_{ij}a_{jk}a_{ki}/3. \quad (27)$$

We evaluate II and III for filter scales  $\Delta/\eta = 32, 64$ , and 128 from the synthetic fields. The overall averages of the quantities as well as the averages conditioned around the saddles and centers are calculated. However, it turns out that the conditional averages are nearly the same as the overall averages. Therefore, only the latter is presented. The data are shown in Fig. 10, where we plot  $(-\text{II}/3)^{1/2}$  against  $(\text{III}/2)^{1/3}$  using the convention in Pope.<sup>15</sup> The data points fall inside the so-called Lumley triangle defined by the solid lines, along the right straight boundary of the triangle. Therefore, the SGS stress tensor tends to have an axisymmetric “cigar” shape.<sup>15,40,41</sup> It thus displays the same trends observed in fully developed pipe flows<sup>39</sup> and isotropic turbulence.<sup>42</sup> (We note that we observe similar trends for the isotropic MTLM synthetic fields. Results are not shown here.) Fig. 10 also indicates that, when the filter scale increases, the SGS stress tensor tends to be more isotropic, with data points moving towards the origin.

#### 5. Small scale intermittency and structures

The above discussion demonstrates that CMTLM fields can capture important effects of large scale structures. The method has yielded these results without compromising the MTLM procedure’s ability to reproduce small scale structures and intermittency. We demonstrate this in this subsection.

Small scale intermittency can be characterized by velocity increments. The longitudinal increment over a displacement  $\mathbf{r}$  is defined as

$$\delta u_r = [\mathbf{u}(\mathbf{x} + \mathbf{r}) - \mathbf{u}(\mathbf{x})] \cdot \mathbf{r}/r, \quad (28)$$



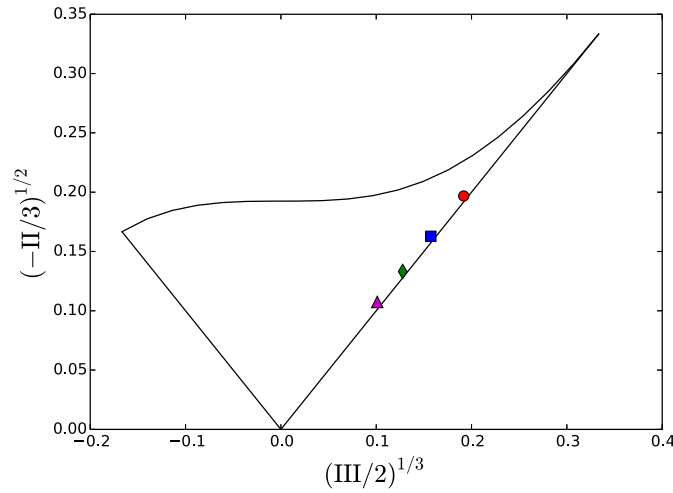


FIG. 10. Anisotropy invariant map for the SGS stress tensor with filter scales  $16\eta$  (circles),  $32\eta$  (squares),  $64\eta$  (diamonds),  $128\eta$  (triangles). The solid lines represent the boundaries of the Lumley triangle.

where  $r = |\mathbf{r}|$  is the magnitude of  $\mathbf{r}$ . Transverse velocity increments can be defined similarly, but for clarity we will discuss only longitudinal ones. When  $r$  is small and well into the dissipation range, the statistics of  $\delta u_r$  become the same as the longitudinal velocity gradient  $\partial_x u$ , and the transverse increment becomes same as the transverse velocity gradient  $\partial_y u$  (for more details, see, e.g., Frisch<sup>44</sup>). Fig. 11 presents the PDFs for  $\delta u_r$  for several values of  $r$ , as well as the PDFs of  $\partial_x u$  and  $\partial_y u$ . As expected, the PDFs show exponential tails when  $r$  is small, an indication of small-scale intermittency. In particular, the PDF of the gradients display stretched-exponential tails. The transverse gradient has wider tails than the longitudinal one. Both are well-known properties in hydrodynamic turbulent flows. The negative skewness in the PDF of the longitudinal gradient and increments is also reproduced. Moreover, the tails of the PDFs become narrower when  $r$  increases, and tend to the Gaussian distribution when  $r$  is large, which is also consistent with observations in real turbulence.

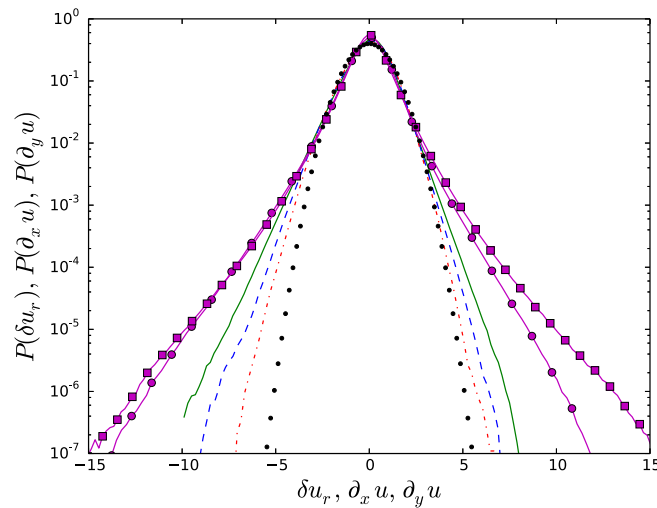


FIG. 11. PDFs of normalized longitudinal velocity increments  $\delta u_r$  (solid line:  $r = 8\eta$ , dashed line:  $r = 16\eta$ , dashed-dotted line:  $r = 32\eta$ ), the longitudinal velocity gradient  $\partial_x u$  (line with circles), and the transverse velocity gradient  $\partial_y u$  (line with squares). Black dots represent the Gaussian distribution.

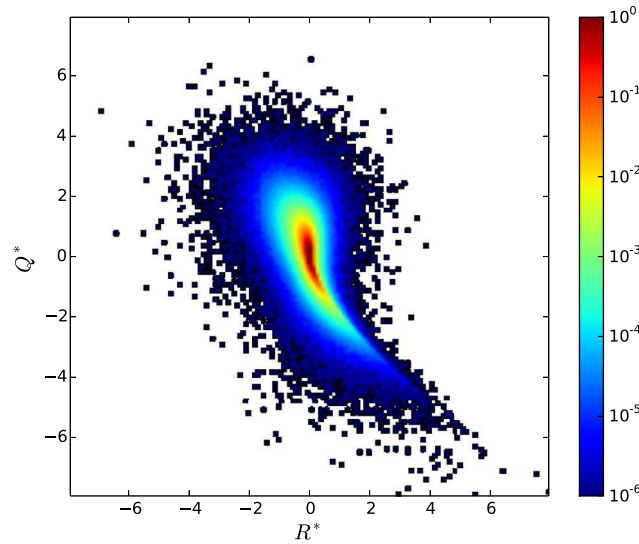


FIG. 12. The joint PDF of the normalized invariants  $Q \equiv -\text{Tr}\mathbf{A}^2/2$  and  $R \equiv -\text{Tr}\mathbf{A}^3/3$ .

The deviation from the Gaussian distribution is quantified by the flatness and the skewness factors. For a variable  $X$ , their definitions are

$$F(X) = \frac{\langle X^4 \rangle}{\langle X^2 \rangle^2}, \quad S(X) = \frac{\langle X^3 \rangle}{\langle X^2 \rangle^{3/2}},$$

respectively. We find that, in the CMTLM fields, the flatness is 5.7 for  $\partial_x u$  and 7.7 for the  $\partial_y u$ . The skewness factor for  $\partial_x u$  is  $-0.45$ . These numbers are in close proximity of the data compiled in previous works<sup>45</sup> for real turbulence.

Another important aspect of small scales of turbulence is their geometrical structures, which can be characterized by the tensor invariants of the velocity gradient tensor  $\mathbf{A}$ , where  $A_{ij} = \partial_j u_i$ . The invariants are denoted as  $Q$  and  $R$ , where<sup>46,47</sup>

$$Q = -\text{Tr}\mathbf{A}^2/2, \quad R = -\text{Tr}\mathbf{A}^3/3.$$

The joint PDF of  $Q$  and  $R$  is shown in Fig. 12, where  $Q$  and  $R$  are normalized by  $\text{Tr}\mathbf{A}\mathbf{A}^T$  and  $(\text{Tr}\mathbf{A}\mathbf{A}^T)^{3/2}$ , respectively. It is clear that the well-known tear-drop shape is reproduced by the contours of the joint PDF. Thus, this and the previous result confirms that CMTLM maintain the desirable properties of the MTLM method while it is able to model additional features in anisotropic flows.

## B. Mean energy balance and Reynolds stress in Kolmogorov flows

In this section, we consider the mean statistics of a Kolmogorov flow simulated using hyperviscosity in Borue and Orszag,<sup>33</sup> and compare the results with the latter.

As is commented in BO,<sup>33</sup> a large ensemble is needed to obtain statistically converged mean statistics. We thus choose a modest resolution with  $128^3$  grid points, and the following analytic expression<sup>37,48</sup> as the prescribed energy spectrum  $E_p(k)$

$$E_p(k) = C_k \epsilon^{2/3} k^{-5/3} \left[ \frac{k\ell}{((k\ell)^{\alpha_2} + \alpha_1)^{1/\alpha_2}} \right]^{5/3 + \alpha_3} \exp(-\alpha_4(k\eta)^{4/3}), \quad (29)$$

where  $C_k = 1.5$  is the Kolmogorov constant,  $\ell \approx 2.07$  is an estimate of the integral length scale. Mean dissipation  $\epsilon$  is specified by  $\epsilon = u_{\text{rms}}^3/\ell$  with  $u_{\text{rms}} = 1.0$ , hence  $\epsilon \approx 0.48$ . The viscosity is chosen such that the Kolmogorov length scale  $\eta = 1.5/k_{\text{max}}$  where  $k_{\text{max}} = 64$  is the maximum wavenumber. As a consequence, the viscosity is  $\nu \approx 0.005$ . The other parameters are  $\alpha_1 = 0.98$ ,  $\alpha_2 = 2$ ,  $\alpha_3 = 4.0$ , and  $\alpha_4 = 2.25$ .

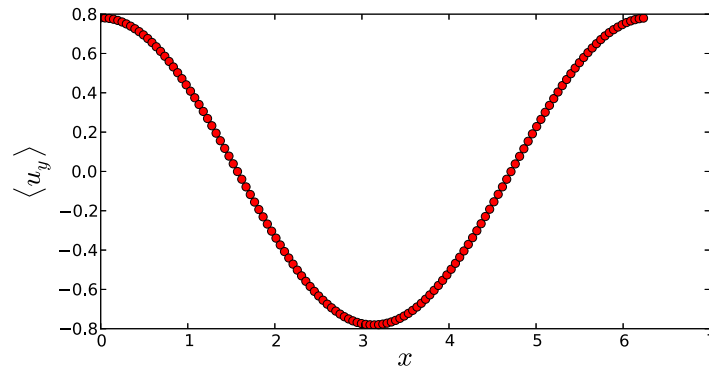


FIG. 13. The mean velocity profile in the synthetic CMTLM fields.

It is well-known that mean statistics such as the production rate of turbulent kinetic energy are flow-dependent, and in particular depend on the specific shape of the low-wavenumber range of the energy spectrum. However, there is no detailed data for the energy spectrum of the present Kolmogorov flow. Given that we will look into the spectral property of the Reynolds stress distribution (see below), it is desirable to extend the inertial range as far as possible. We thus choose to use the above analytic spectrum, even though it does not capture the production range of the spectrum of flow realistically. The parameters in the spectrum are chosen to extend the inertial range, hence produce only a narrow production range and an under-resolved dissipation range. As a consequence, we will mainly focus on the spatial dependence of the statistics. Nevertheless, the magnitudes of most of the statistics are consistent with those in BO,<sup>33</sup> except that the energy dissipation is over-predicted as is shown below.

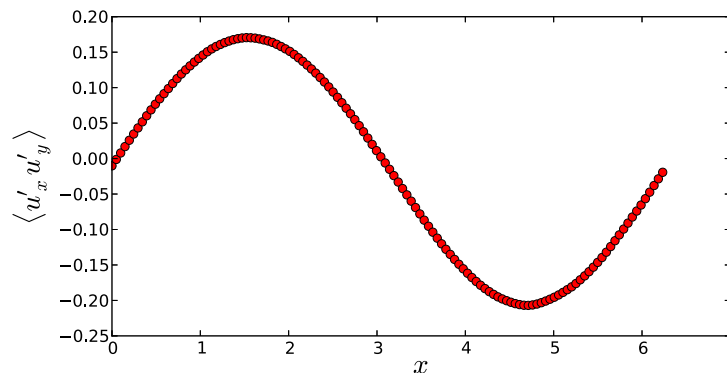
The DNS in BO<sup>33</sup> produces a mean velocity profile as follows:

$$u_x = 0, u_y = A \cos(k_f x), u_z = 0, \quad (30)$$

where  $k_f = 1$  and  $A$  is a constant. We set the mean profile as the target field for the CMTLM fields. As a consequence,  $\Omega = (1, 0, 0)$ .  $\mathcal{F}$  is defined as in Sec. IV A, i.e.,  $\mathcal{F} = 1$  on  $\Omega$  and 0 otherwise. We set  $A = 0.4$ .

Using tolerance  $e = 10\%$ , we generate more than 2000 CMTLM fields. The statistics are averaged over all the fields as well as the  $y$  and  $z$  directions. The mean velocity generated by the CMTLM procedure is plotted in Fig. 13, which reproduces the target field we have specified.

The flow field allows non-trivial distribution for the Reynolds stress component  $R_{xy} = \langle u'_x u'_y \rangle$ , where  $u'_x = u_x - \langle u_x \rangle$  is the fluctuation of the  $x$ -component of the velocity, and similarly for  $u'_y$ .  $R_{xy}$  as a function of  $x$  is plotted in Fig. 14. It has a sinusoidal distribution with a  $\pi/2$  phase-shift from the mean velocity profile. The distribution reproduces very well the DNS result reported in BO.<sup>33</sup>

FIG. 14. The Reynolds stress  $\langle u'_x u'_y \rangle$  in the synthetic CMTLM fields.

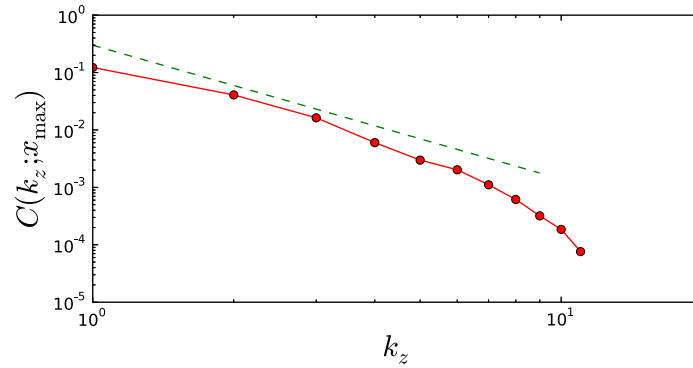


FIG. 15. The one-dimensional co-spectrum  $C(k_z; x_{\max})$  in the CMTLM fields (solid line with circles) as a function of the  $k_z$  component of the wavenumber, which is evaluated at  $x_{\max} = 3\pi/2$  where the mean shear is the strongest. The dashed line has slope  $k_z^{-7/3}$ .

We note that this result is non-trivial, since we only use the mean velocity field as the target field in our optimization. The Reynolds stress distribution is generated by the MTLM procedure coupled with the optimization process.

The distribution of mean Reynolds stress over different length scales can be characterized by the co-spectrum of  $u_x$  and  $u_y$ . We use the one-dimensional co-spectrum  $C(k_z; x)$  defined as

$$C(k_z; x) = \text{Re}\{\langle \hat{u}_x(x, y, k_z) \hat{u}_y^*(x, y, k_z) \rangle\},$$

where  $\text{Re}\{\cdot\}$  denotes the real part, and  $\hat{u}_x(x, y, k_z)$  is the one-dimensional Fourier transform of  $u_x$  and similarly for  $\hat{u}_y$ . The average is taken over different realizations and the  $y$  direction.  $C(k_z; x)$  is a function of  $x$  as the mean Reynolds stress depends on  $x$ . For high Reynolds number turbulence with characteristic mean shear  $\mathcal{S}$ ,  $C(k_z; x)$  is predicted dimensionally to scale with  $\mathcal{S}\epsilon^{1/3}k^{-7/3}$  for wavenumber  $k < k_s = \mathcal{S}^{3/2}/\epsilon^{1/2}$  but large compared with the wavenumbers characterizing the integral scales.<sup>15,33,49</sup> In the DNS study by BO,<sup>33</sup> a short scaling range has been observed for  $C(k_z; x)$ . The result for the CMTLM fields is plotted in Fig. 15 for  $x = 3\pi/2$  where the mean shear  $\partial\langle u_y \rangle/\partial x$  is the maximum. Given the moderate Reynolds number of the fields, only approximate scaling is observed. Nevertheless, the result is consistent with a  $k_z^{-7/3}$  spectrum and the hyperviscosity DNS results.<sup>33</sup>

The distribution of mean turbulent kinetic energy  $K \equiv \langle u'_i u'_i \rangle / 2$  is shown in Fig. 16. Apart from small deviation due to statistical fluctuations, the distribution has a periodic distribution with period  $\pi$ , which agrees with observations in DNS.<sup>33</sup> The kinetic energy distribution is determined by the

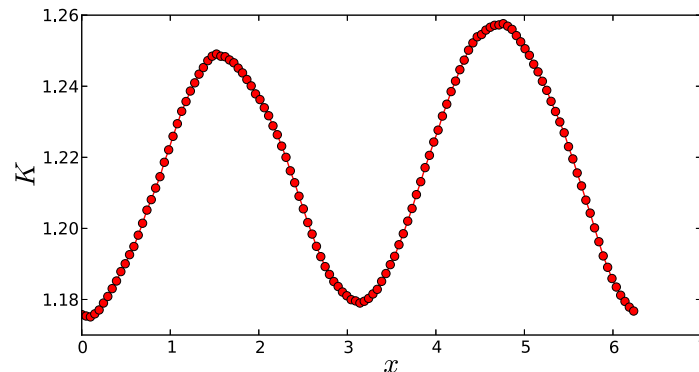


FIG. 16. The mean turbulent kinetic energy  $K$  in the CMTLM fields.

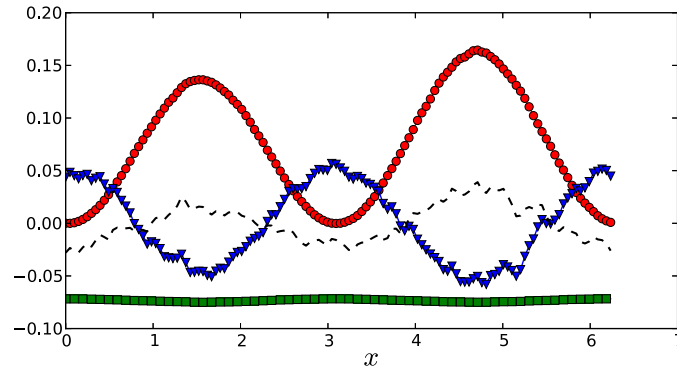


FIG. 17. Terms in turbulent kinetic energy balance in the synthetic CMTLM fields. Circles: production term  $P$ ; gradients: transport term  $T$ ; squares: rescaled turbulent energy dissipation  $-D$  (see text); dashed line: sum of the three terms.

turbulent energy production  $P$ , turbulent transport  $T$ , and turbulent energy dissipation  $D$ , where

$$T = -\frac{\partial}{\partial x_i} \left[ \left\langle u'_i \frac{u'_j u'_j}{2} \right\rangle + \langle u'_i p' \rangle - \nu \frac{\partial K}{\partial x_i} \right], \quad (31)$$

$$P = -\langle u'_i u'_j \rangle \frac{\partial \langle u_i \rangle}{\partial x_j}, \quad (32)$$

$$D = \nu \langle \partial_j u'_i \partial_j u'_i \rangle, \quad (33)$$

in which  $p' \equiv p - \langle p \rangle$  is the pressure fluctuation. The constant density has been assumed to be unit. In the statistically stationary turbulence, we have

$$T + P - D = 0.$$

$T$  and  $P$ , as well as a rescaled  $-D$  term, are plotted in Fig. 17 for the CMTLM fields. The sinusoidal distributions for  $P$  and  $T$  follow closely DNS results.<sup>33</sup> In particular, the transport term  $T$  counteracts with the production term  $P$ , but with smaller amplitude. In BO,<sup>33</sup> it is shown that the difference is made up for by the turbulent dissipation term  $D$ . Hence,  $D$  also has a sinusoidal distribution. In the CMTLM field, we also observe sinusoidal distribution for  $D$ . However, its magnitude is over-predicted, because the analytic spectrum does not resolve the dissipation range as explained previously. To illustrate the distribution of  $D$ , we rescale it with a scaling factor defined as  $(\overline{T} + \overline{P})/\overline{D}$ , where overbar denotes averaging over the  $x$  direction. The rescaled turbulent dissipation thus on average equals the sum of the production and transport terms. For the current CMTLM fields, the value for the factor is approximately 0.07. The (minus) rescaled  $D$  is shown in Fig. 17 with squares. It indeed displays the weak oscillatory behavior observed in DNS. The sum of the three terms is shown by the dashed line, which oscillates with a small amplitude around zero. It confirms that the dissipation term tends to balance the combined effects of the other two terms, even though there is still some discrepancy in the magnitudes.

## V. CONCLUSIONS

We introduce a new technique in this paper to generate anisotropic synthetic turbulence. The technique generalizes the MTLM, and is named the CMTLM. In this method, we adjust the random input to the map so that the output contains the large scale anisotropic structures we aim for. After the MTLM procedure is slightly simplified, we derive the optimality system corresponding to the mapping, and show that the adjustment can be accomplished by an adjoint-based optimization process.

We then apply the method to synthesize two Kolmogorov flows, in which the mean flows are known and set as the target fields. Direct numerical simulations have shown that the persistent large

scale structures in such flows lead to non-trivial mean flow statistics, and also have significant effects on the small scale motions. We look into the anisotropic distribution in subgrid-scale dissipation, the alignment between the subgrid-scale stress and the filtered strain rate tensor, the mean Reynolds stress, and mean turbulent kinetic energy budget, among others, in the synthetic fields. Comparing with direct numerical simulations, we observe that the synthetic fields capture the effects with very good qualitative agreement.

Our calculations show that the method is cost efficient and almost always converges in few (less than 10) iterations to within a 3% tolerance. It also appears to be more flexible than some of the previous techniques. In principle, additional flow features can easily be incorporated where needed. For example, the distribution of the Reynolds stress tensor can be imposed as a constraint if precise values are required. The procedure could also be generalized to synthetic scalar fields. On the other hand, it is desirable to implement the method with a simulation code to verify its benefits *a posteriori*. These ideas and other possible generalizations are the topics of future research.

## ACKNOWLEDGMENTS

We gratefully acknowledge the support by the Royal Society (Grant No. TG090539). Y.L. also thanks Dr. Willis and Professor Ohkitani for stimulating discussions.

## APPENDIX: EXPRESSIONS FOR THE OPERATORS

The derivation in the main text has shown that the following integral:

$$I = \int \xi \cdot \mathcal{M} \phi d^3 \mathbf{x} \quad (\text{A1})$$

appears in functional derivatives such as  $\delta \mathcal{L} / \delta \phi$  and  $\mathcal{D}J / \mathcal{D} \phi$ . Thus, we evaluate the variation of  $I$ ,  $\delta I$ , with respect to  $\delta \phi$ , the variation of  $\phi$ .

Let  $\delta \mathbf{u}_{n0}$  be the variation of  $\mathbf{u}_{n0}$  corresponding to  $\delta \phi$ . Using Eq. (5), we find

$$\begin{aligned} \delta \mathbf{u}_{(n+1)0} &= \delta [\mathcal{R}_n (\mathcal{P} \mathcal{A}_n)^{m_n} \mathcal{G}_n + \mathcal{G}_n^c] \mathbf{u}_{n0}. \\ &= \delta [\mathcal{R}_n \mathbf{u}_{n2}] + \mathcal{G}_n^c \delta \mathbf{u}_{n0} \\ &= \mathcal{D}_n^R \delta \mathbf{u}_{n2} + \mathcal{G}_n^c \delta \mathbf{u}_{n0}. \end{aligned} \quad (\text{A2})$$

Operator  $\mathcal{D}_n^R$  is the linearization of  $\mathcal{R}_n$ .  $\mathcal{D}_n^R$  itself depends on  $\mathbf{u}_{n2}$ . The second term follows from the linearity of filter  $\mathcal{G}_n^c$ .  $\delta \mathbf{u}_{n2}$  is the variation of  $\mathbf{u}_{n2}$ .

Note  $\mathbf{u}_{n2} = (\mathcal{P} \mathcal{A}_n)^{m_n} \mathbf{u}_{n1}$ . We introduce the following notations:

$$\mathbf{v}_{ni} = (\mathcal{P} \mathcal{A}_n)^i \mathbf{u}_{n1}, \quad (\text{A3})$$

for  $i = 0, 1, \dots, m_n - 1$ , where  $\mathbf{v}_{n0} \equiv \mathbf{u}_{n1}$ . Thus,

$$\begin{aligned} \delta \mathbf{u}_{n2} &= \delta (\mathcal{P} \mathcal{A}_n \mathbf{v}_{n(m_n-1)}) \\ &= \mathcal{D}_{n(m_n-1)}^A \delta \mathbf{v}_{n(m_n-1)}, \end{aligned} \quad (\text{A4})$$

where  $\mathcal{D}_{n(m_n-1)}^A$  is the linearization of operator  $\mathcal{P} \mathcal{A}_n$  when the latter is applied to  $\mathbf{v}_{n(m_n-1)}$ . The subscript of  $\mathcal{D}_{n(m_n-1)}^A$  emphasizes that it depends on  $\mathbf{v}_{n(m_n-1)}$ .

Given that  $\mathbf{v}_{ni} = \mathcal{P} \mathcal{A}_n \mathbf{v}_{n(i-1)}$ , the above derivation can be repeated, leading to

$$\delta \mathbf{u}_{n2} = \mathcal{D}_{n(m_n-1)}^A \mathcal{D}_{n(m_n-2)}^A \cdots \mathcal{D}_{n0}^A \delta \mathbf{u}_{n1}. \quad (\text{A5})$$

Let

$$\mathcal{D}_n^A = \mathcal{D}_{n(m_n-1)}^A \mathcal{D}_{n(m_n-2)}^A \cdots \mathcal{D}_{n0}^A, \quad (\text{A6})$$

we have

$$\delta \mathbf{u}_{n2} = \mathcal{D}_n^A \delta \mathbf{u}_{n1} = \mathcal{D}_n^A \mathcal{G}_n \delta \mathbf{u}_{n0}. \quad (\text{A7})$$

Thus, we find

$$\delta \mathbf{u}_{(n+1)0} = (\mathcal{D}_n^R \mathcal{D}_n^A \mathcal{G}_n + \mathcal{G}_n^c) \delta \mathbf{u}_{n0}. \quad (\text{A8})$$

Therefore,

$$\begin{aligned} \delta I &= \int \boldsymbol{\xi} \cdot (\mathcal{D}_M^R \mathcal{D}_M^A \mathcal{G}_M + \mathcal{G}_M^c) \delta \mathbf{u}_{M0} d^3 \mathbf{x} \\ &= \int (\mathcal{G}_M \mathcal{D}_M^{A+} \mathcal{D}_M^{R+} + \mathcal{G}_M^c) \boldsymbol{\xi} \cdot \delta \mathbf{u}_{M0} d^3 \mathbf{x} \\ &= \int (\mathcal{B}_M + \mathcal{G}_M^c) \boldsymbol{\xi} \cdot \delta \mathbf{u}_{M0} d^3 \mathbf{x}, \end{aligned} \quad (\text{A9})$$

where we have used the fact that  $\mathcal{G}_n$  and  $\mathcal{G}_n^c$  are self-adjoint. Repeating the above derivation, we find

$$\begin{aligned} \delta I &= \int \prod_{n=1}^M (\mathcal{B}_n + \mathcal{G}_n^c) \boldsymbol{\xi} \cdot \delta \mathbf{u}_{10} d^3 \mathbf{x} \\ &= \int \mathcal{P} \prod_{n=1}^M (\mathcal{B}_n + \mathcal{G}_n^c) \boldsymbol{\xi} \cdot \delta \boldsymbol{\varphi} d^3 \mathbf{x}, \end{aligned} \quad (\text{A10})$$

where the product is ordered with  $n$  increasing from left to right. The facts that  $\delta \mathbf{u}_{10} = \mathcal{P} \delta \boldsymbol{\varphi}$  and that  $\mathcal{P}$  is self-adjoint have been applied. Hence,

$$\begin{aligned} \frac{\delta I}{\delta \boldsymbol{\varphi}} &= \int \boldsymbol{\xi} \cdot \frac{\delta \mathcal{M} \boldsymbol{\varphi}}{\delta \boldsymbol{\varphi}} d^3 \mathbf{x} \\ &= \mathcal{P} \prod_{n=1}^M (\mathcal{B}_n + \mathcal{G}_n^c) \boldsymbol{\xi} \equiv \mathcal{M}^+ \boldsymbol{\xi}, \end{aligned} \quad (\text{A11})$$

Eq. (A11) gives the definition of  $\mathcal{M}^+$ . Using Eqs. (13) and (17), we thus find

$$\frac{\mathcal{D}J}{\mathcal{D}\boldsymbol{\varphi}} = \left. \frac{\delta \mathcal{L}}{\delta \boldsymbol{\varphi}} \right|_{\mathbf{u}_e, \boldsymbol{\xi}} = -\mathcal{M}^+ \boldsymbol{\xi}. \quad (\text{A12})$$

$\mathcal{M}^+$  has the following equivalent form:

$$\mathcal{M}^+ = \mathcal{P} \sum_{i=1}^M \mathcal{G}_{i-1}^c \prod_{n=i}^M \mathcal{B}_n. \quad (\text{A13})$$

It can be shown by expanding the product in Eq. (A11), and noting  $\mathcal{G}_{n-1}^c \mathcal{G}_n^c = \mathcal{G}_n^c$ , and  $\mathcal{B}_{n-1} \mathcal{G}_n^c = 0$ . As is shown in the main text, this expression allows us to calculate  $\mathcal{M}^+ \boldsymbol{\xi}$  via an iteration symmetrical to the MTLM procedure.

It remains to derive the expressions for  $\mathcal{D}_n^{R+}$  and  $\mathcal{D}_n^{A+}$ . We outline the main steps of the derivations.

To find  $\mathcal{D}_u^{R+}$ , we start with  $\mathcal{R}_u$ , namely,  $\mathcal{R}$  acting on a generic velocity field  $\mathbf{u}$ . Using the definition of  $\mathcal{R}$  [Eq. (4)], it is not difficult to find the variation  $\delta(\mathcal{R}_u \mathbf{u})$ , hence  $\mathcal{D}_u^R \delta \mathbf{u}$ , which gives us the expression of  $\mathcal{D}_u^R$ . We then form the following inner product:

$$I_R = \int \boldsymbol{\eta}(\mathbf{x}) \cdot \mathcal{D}_u^R \delta \mathbf{u}(\mathbf{x}) d^3 \mathbf{x}, \quad (\text{A14})$$

where  $\boldsymbol{\eta}(\mathbf{x})$  is a test function. The action of  $\mathcal{D}_u^{R+}$  on  $\boldsymbol{\eta}$  is then found by integration by parts, which gives the definition of  $\mathcal{D}_u^{R+}$ . In Fourier space, the result can be written as

$$\mathcal{D}_u^{R+} \hat{\boldsymbol{\eta}}(\mathbf{k}) = \mathcal{R}_u \hat{\boldsymbol{\eta}}(\mathbf{k}) - \frac{E_p(k)^{1/2}}{E_u(k)^{3/2}} \zeta_{u\eta}(k) \hat{\mathbf{u}}(\mathbf{k}), \quad (\text{A15})$$



where  $\hat{\eta}$  is the Fourier transform of  $\eta$ , and  $\zeta_{u\eta}(k)$  is the co-spectrum between  $\mathbf{u}$  and  $\eta$ , defined as

$$\zeta_{u\eta}(k) = \frac{1}{2} \oint_{S_k} \hat{\eta}^* \cdot \hat{\mathbf{u}} dS, \quad (\text{A16})$$

where the integral is conducted over the spherical surface  $S_k = \{\mathbf{k}: |\mathbf{k}| = k\}$  in the Fourier space, and the asterisk denotes complex conjugate.  $\mathcal{D}_n^{R+}$  is simply  $\mathcal{D}_u^{R+}$  with  $\mathbf{u}$  replaced by  $\mathbf{u}_{n2}$ .

As for  $\mathcal{D}_n^{A+}$ , in light of Eq. (A6), we have

$$\mathcal{D}_n^{A+} = \mathcal{D}_{n0}^{A+} \mathcal{D}_{n1}^{A+} \dots \mathcal{D}_{n(m_n-1)}^{A+}. \quad (\text{A17})$$

Therefore, we need to find  $\mathcal{D}_{ni}^{A+}$  in order to find  $\mathcal{D}_n^{A+}$ . We consider  $\mathcal{D}_u^{A+}$ , which is defined as the adjoint of the linearization of  $\mathcal{PA}$  when the latter is applied to a generic function  $\mathbf{u}$ . In other words,  $\mathcal{D}_u^{A+}$  is the same as  $\mathcal{D}_{ni}^{A+}$  with  $\mathbf{v}_{ni}$  replaced by  $\mathbf{u}$ . Following the same ideas presented above, we can derive the expression for  $\mathcal{D}_u^{A+}$  acting on the test function  $\eta(\mathbf{x})$

$$\begin{aligned} \mathcal{D}_u^{A+} \eta(\mathbf{x}) &= \int d^3\mathbf{y} W(\mathbf{y} - \mathbf{x} - \mathbf{u}(\mathbf{x})t) \mathcal{P}\eta(\mathbf{y}) \\ &+ \int d^3\mathbf{y} W(\mathbf{y} - \mathbf{x} - \mathbf{u}(\mathbf{x})t) [\nabla_{\mathbf{y}} \mathcal{P}\eta(\mathbf{y})] \cdot \mathbf{u}(\mathbf{x})t, \end{aligned} \quad (\text{A18})$$

in which  $W(\cdot)$  is the same weight function used in the MTLM procedure, and  $t$  is the advection time parameter.  $\nabla_{\mathbf{y}}$  denotes the gradient operator with  $\mathbf{y}$  as the variables.

$\mathcal{D}_u^{R+}$  and  $\mathcal{D}_u^{A+}$  both depend on  $\mathbf{u}$ . Thus, in order to find  $\mathcal{M}^+\xi$ , we need velocity fields  $\mathbf{v}_{ni}$  for  $i = 0, 1, \dots, m_n - 1$ , and  $\mathbf{u}_{n2}$ . They are found and stored during the solution of the state equation [Eq. (6)].

- <sup>1</sup> A. Juneja, D. P. Lathrop, K. R. Sreenivasan, and G. Stolovitzky, "Synthetic turbulence," *Phys. Rev. E* **49**, 5179–5194 (1994).
- <sup>2</sup> A. Arneodo, E. Bacry, and J. F. Muzy, "Random cascades on wavelet dyadic trees," *J. Math. Phys.* **39**, 4142–1998 (1998).
- <sup>3</sup> A. Scotti and C. Meneveau, "Fractal model for coarse-grained nonlinear partial differential equation," *Phys. Rev. Lett.* **78**, 867 (1997).
- <sup>4</sup> A. Scotti and C. Meneveau, "A fractal model for large eddy simulation of turbulent flow," *Physica D* **127**, 198–232 (1999).
- <sup>5</sup> J. C. H. Fung, J. C. R. Hunt, N. A. Malik, and R. J. Perkins, "Kinematic simulation of homogeneous turbulence by unsteady random Fourier modes," *J. Fluid Mech.* **236**, 281–318 (1992).
- <sup>6</sup> J. C. H. Fung and J. C. Vassilicos, "Two-particle dispersion in turbulentlike flows," *Phys. Rev. E* **57**(2), 1677–1690 (1998).
- <sup>7</sup> C. Cambon, F. S. Godeferd, F. C. G. Nicolleau, and J. C. Vassilicos, "Turbulent diffusion in rapidly rotating flows with and without stable stratification," *J. Fluid Mech.* **499**, 231–255 (2004).
- <sup>8</sup> A. Keating, U. Piomelli, E. Balaras, and H.-J. Kaltenbach, "A priori and a posteriori tests of inflow conditions for large-eddy simulation," *Phys. Fluids* **16**, 4696–4712 (2004).
- <sup>9</sup> G. R. Tabor and M. H. Baba-Ahmadi, "Inlet conditions for large eddy simulation: A review," *Comput. Fluids* **39**, 553–567 (2010).
- <sup>10</sup> C. W. Li and J. H. Wang, "Large eddy simulation of free surface shallow-water flow," *Int. J. Numer. Methods Fluids* **34**, 31–46 (2000).
- <sup>11</sup> C. Bogey and C. Bailly, "Effects of inflow conditions and forcing on subsonic jet flows and noise," *AIAA J.* **43**, 1000–1007 (2005).
- <sup>12</sup> A. Smirnov, S. Shi, and I. Celik, "Random flow generation technique for large eddy simulations and particle-dynamics modeling," *J. Fluids Eng.* **123**, 359–371 (2001).
- <sup>13</sup> P. Batten, U. Goldberg, and S. Chakravarthy, "Interfacing statistical turbulence closures with large-eddy simulation," *AIAA J.* **42**(3), 485–492 (2004).
- <sup>14</sup> L. Davidson and M. Billson, "Hybrid LES-RANS using synthesized turbulent fluctuations for forcing in the interface region," *Int. J. Heat Fluid Flow* **27**, 1028–1042 (2006).
- <sup>15</sup> S. B. Pope, *Turbulent Flows* (Cambridge University Press, Cambridge, 2000).
- <sup>16</sup> S. Lee, S. K. Lele, and P. Moin, "Simulation of spatially evolving turbulence and the applicability of Taylor's hypothesis in compressible flow," *Phys. Fluids A* **4**(7), 1521–1530 (1992).
- <sup>17</sup> H. Le, P. Moin, and J. Kim, "Direct numerical simulation of turbulent flow over a backward-facing step," *J. Fluid Mech.* **330**, 349–374 (1997).
- <sup>18</sup> H.-J. Kaltenbach and G. Janke, *Phys. Fluids* **12**(9), 2320–2337 (2000).
- <sup>19</sup> M. Klein, A. Sadiki, and J. Janicka, "A digital filter based generation of inflow data for spatially developing direct numerical or large eddy simulations," *J. Comput. Phys.* **186**, 652–665 (2003).
- <sup>20</sup> L. di Mare, M. Klein, W. P. Jones, and J. Janicka, "Synthetic turbulence inflow conditions for large-eddy simulation," *Phys. Fluids* **18**, 025107 (2006).
- <sup>21</sup> S. Benhamadouche, N. Jarrin, Y. Addad, and D. Laurence, "Synthetic turbulent inflow conditions based on a vortex method for large-eddy simulation," *Prog. Comput. Fluid Dyn.* **6**, 50–57 (2006).

- <sup>22</sup> N. Jarrin, S. Benhamadouche, D. Laurence, and R. Prosser, "A synthetic-eddy-method for generating inflow conditions for large-eddy simulations," *Int. J. Heat Fluid Flow* **27**, 585–593 (2006).
- <sup>23</sup> M. Pamiés, P.-E. Weiss, E. Garnier, S. Deck, and P. Sagaut, "Generation of synthetic turbulent inflow data for large eddy simulation of spatially evolving wall-bounded flows," *Phys. Fluids* **21**, 045103 (2009).
- <sup>24</sup> N. Jarrin, R. Prosser, J.-C. Uribe, S. Benhamadouche, and D. Laurence, "Reconstruction of turbulent fluctuations for hybrid RANS/LES simulations using a synthetic-eddy method," *Int. J. Heat Fluid Flow* **30**, 435–442 (2009).
- <sup>25</sup> C. Rosales and C. Meneveau, "A minimal multiscale Lagrangian map approach to synthesize non-Gaussian turbulent vector fields," *Phys. Fluids* **18**, 075104 (2006).
- <sup>26</sup> C. Rosales and C. Meneveau, "Anomalous scaling and intermittency in three-dimensional synthetic turbulence," *Phys. Rev. E* **78**, 016313 (2008).
- <sup>27</sup> Y. Li and C. Meneveau, "Origin of non-Gaussian statistics in hydrodynamic turbulence," *Phys. Rev. Lett.* **95**, 164502 (2005).
- <sup>28</sup> Y. Li and C. Meneveau, "Intermittency trends and Lagrangian evolution of non-Gaussian statistics in turbulent flow and scalar transport," *J. Fluid Mech.* **558**, 133–142 (2006).
- <sup>29</sup> C. Rosales, "Synthetic three-dimensional turbulent passive scalar fields via the minimal Lagrangian map," *Phys. Fluids* **23**(7), 075106 (2011).
- <sup>30</sup> L. Chevillard, E. Leveque, F. Taddia, C. Meneveau, H. Yu, and C. Rosales, "Local and nonlocal pressure Hessian effects in real and synthetic fluid turbulence," *Phys. Fluids* **23**, 095108 (2011).
- <sup>31</sup> M. D. Gunzburger, *Perspectives in Flow Control and Optimization* (SIAM, 2003).
- <sup>32</sup> H. S. Kang and C. Meneveau, "Effect of large-scale coherent structures on subgrid-scale stress and strain-rate eigenvector alignments in turbulent shear flow," *Phys. Fluids* **17**, 055103 (2005).
- <sup>33</sup> V. Borue and S. A. Orszag, "Numerical study of three-dimensional Kolmogorov flow at high Reynolds numbers," *J. Fluid Mech.* **306**, 293–323 (1996).
- <sup>34</sup> C. Meneveau and J. Katz, "Scale-invariance and turbulence models for large-eddy simulation," *Annu. Rev. Fluid Mech.* **32**, 1–32 (2000).
- <sup>35</sup> U. Piomelli, W. H. Cabot, P. Moin, and S. Lee, "Subgrid-scale backscatter in turbulent and transitional flows," *Phys. Fluids A* **3**, 1766–1771 (1991).
- <sup>36</sup> C. Hartel, L. Kleiser, F. Unger, and R. Friedrich, "Subgrid-scale energy transfer in the near-wall region of turbulent flows," *Phys. Fluids* **6**, 3130–3143 (1994).
- <sup>37</sup> H. S. Kang, S. Chester, and C. Meneveau, "Decaying turbulence in an active-grid-generated flow and comparisons with large-eddy simulation," *J. Fluid Mech.* **480**, 129–160 (2003).
- <sup>38</sup> T. S. Lund and M. M. Rogers, "An improved measure of strain state probability in turbulent flows," *Phys. Fluids* **6**, 1838–1847 (1994).
- <sup>39</sup> C. Brun, R. Friedrich, and C. B. da Silva, "A non-linear SGS model based on the spatial velocity increment," *Theor. Comput. Fluid Dyn.* **20**, 1–21 (2006).
- <sup>40</sup> J. L. Lumley, "Computational modelling of turbulent flows," *Adv. Appl. Mech.* **18**, 123–176 (1978).
- <sup>41</sup> A. J. Simonsen and P. A. Krogstad, "Turbulent stress invariant analysis: Clarification of existing terminology," *Phys. Fluids* **17**, 088103 (2005).
- <sup>42</sup> B. Tao, J. Katz, and C. Meneveau, "Statistical geometry of subgrid-scale stresses determined from holographic particle image velocimetry measurements," *J. Fluid Mech.* **457**, 35–78 (2002).
- <sup>43</sup> K. Horiuti, "Roles of non-aligned eigenvectors of strain-rate and subgrid-scale stress tensors in turbulence generation," *J. Fluid Mech.* **491**, 65–100 (2003).
- <sup>44</sup> U. Frisch, *Turbulence: The Legacy of A. N. Kolmogorov* (Cambridge University Press, Cambridge, 1995).
- <sup>45</sup> K. R. Sreenivasan and R. A. Antonia, "The phenomenology of small-scale turbulence," *Annu. Rev. Fluid Mech.* **29**, 435–472 (1997).
- <sup>46</sup> B. J. Cantwell, "Exact solution of a restricted Euler equation for the velocity gradient tensor," *Phys. Fluids A* **4**, 782–793 (1992).
- <sup>47</sup> C. Meneveau, "Lagrangian dynamics and models of the velocity gradient tensor in turbulent flows," *Annu. Rev. Fluid Mech.* **43**, 219–245 (2011).
- <sup>48</sup> Y.-H. Pao, "Structure of turbulent velocity and scalar fields at large wavenumbers," *Phys. Fluids* **8**, 1063–1075 (1965).
- <sup>49</sup> J. L. Lumley, "Similarity and turbulent energy spectrum," *Phys. Fluids* **10**, 855 (1967).